Nonlinear Behavior of Space Shuttle Superlightweight Tank Under Booster Ascent Loads

Richard D. Young,[*] Michael P. Nemeth,[†] Timothy J. Collins,[‡] and James H. Starnes Jr.[§]
NASA Langley Research Center, Hampton, Virginia 23681-2199

Results of linear-bifurcation and nonlinear analyses of the Space Shuttle superlightweight (SLWT) external liquid-oxygen (LO$_2$) tank for an important early booster ascent loading condition are presented. These results for thin-walled linear elastic shells that are subjected to combined mechanical and thermal loads illustrate an important type of response mode that may be encountered in the design of other liquid-fuel launch vehicles. Linear-bifurcation analyses are presented that predict several nearly equal eigenvalues that correspond to local buckling modes in the forward ogive section of the LO$_2$ tank. In contrast, the nonlinear response phenomenon is shown to consist of short-wavelength bending deformations in the forward-ogive and barrel sections of the LO$_2$ tank that grow in amplitude in a stable manner with increasing load. Imperfection sensitivity analyses are presented that show that the presence of several nearly equal eigenvalues does not lead to a premature general instability mode for the forward-ogive section. For the linear-bifurcation and nonlinear analyses, the results show that accurate predictions of the response of the shell generally require a large-scale, high-fidelity, finite element model, and that a design based on a linear-bifurcation buckling analysis and a buckling-load knockdown factor is overly conservative. Results are presented that show that the SLWT LO$_2$ tank can support loads in excess of approximately 2.6 times the values of the operational loads considered. In addition, results are presented that show that local bending deformations may cause failure of the thermal protection system (TPS) at load levels less than the load level corresponding to structural collapse. Results are presented that can be used to estimate the load level at which TPS failure is likely to occur.

Introduction

THE International Space Station (ISS) is currently planned to occupy a 51.6-deg orbit. Construction of the ISS will require the Space Shuttle to deliver a large number of payloads to this high-inclination orbit. However, achieving this orbit requires that the payload capacity of the orbiter be reduced by approximately 10,000 lb. To recover part of this lost payload capacity, and to minimize the number of Space Shuttle flights needed to build the ISS, NASA developed a new lighter weight external fuel tank for the Space Shuttle. This new design, referred to as the superlightweight (SLWT) external tank, is made primarily of an aluminum–lithium alloy and weighs approximately 58,000 lb, which is approximately 8000 lb lighter than the lightweight aluminum external tank previously in service. This 8000-lb weight savings translates into an 8000-lb increase in the payload capacity for the orbiter. The new SLWT tank flew for the first time on 2 June 1998 (Space Transportation System-mission 91).

An important consideration in the design of the SLWT tank is the nonlinear behavior of its thin-walled regions that experience compressive or shear stresses and the sensitivity of this behavior to initial geometric imperfections. Small initial geometric imperfections are known to sometimes cause premature buckling of thin shell structures. These effects are very important in the present study because local or global buckling of the SLWT tank shell wall could lead to catastrophic structural collapse or cause the thermal protection system (TPS) to separate from the tank, which could also cause the vehicle to fail. To eliminate shell-wall instabilities for operational loads, accurate predictions of the nonlinear response and imperfection sensitivity of the SLWT tank are needed. However,

obtaining this information is a significant task. For example, accurate predictions of the nonlinear response of the SLWT tank have been shown in Ref. 1 to require a large-scale, high-fidelity, finite element model to represent complex structural details and a robust nonlinear shell analysis capability that can predict local and general instability buckling modes.

One thin-walled component of the SLWT tank that experiences significant compressive stresses is the liquid-oxygen (LO$_2$) tank (see Fig. 1). Prior to launch, the weights of the liquid-hydrogen (LH$_2$) tank, the LO$_2$ tank, and the fuel induce reactions at the solid-rocket-booster (SRB) attachment points that cause meridional compressive stresses and shear stresses that extend into the nose of the SLWT tank. The nonlinear behavior of the SLWT LO$_2$ tank subjected to two critical prelaunch loading conditions has been documented extensively in Refs. 1 and 2. The tank also experiences similar compressive and shear stresses during ascent, before the two SRBs are jettisoned. After the SRBs are jettisoned, and prior to orbital insertion, the LO$_2$ tank experiences compressive stresses in the aft end of the tank instead of in the nose region.

This paper presents results of elastic linear-bifurcation and nonlinear analyses of the LO$_2$ tank that were conducted at the NASA Langley Research Center. The results are for a critical flight loading condition that occurs 69.66 s into the flight, during ascent, before the SRBs are jettisoned (referred to herein as the early booster ascent loading condition). Two primary objectives of the present paper are to describe the nonlinear response phenomena for this loading condition and to determine how much additional load beyond the operational load level the LO$_2$ tank can withstand before collapsing or exhibiting wrinklelike bending deformations that can lead to failure of the TPS. These objectives are accomplished for this early booster ascent loading condition by using the large-scale, finite element analysis approach of Refs. 1 and 2, in which results were presented for two full-scale structural tests that suggested that the finite element modeling approach was adequate for representing the nonlinear behavior of the SLWT LO$_2$ tank for the two prelaunch loading conditions considered in Refs. 1 and 2. As part of this analysis approach, results will be presented that assess the relevance of linear-bifurcation buckling analyses of the present vehicle and provide insight into the performance of the TPS. By presenting specific results for the present vehicle and loading condition, the present

[*]Aerospace Engineer, Structural Mechanics Branch. Member AIAA.
[†]Senior Research Engineer, Structural Mechanics Branch. Associate Fellow AIAA.
[‡]Aerospace Engineer, Structural Mechanics Branch.
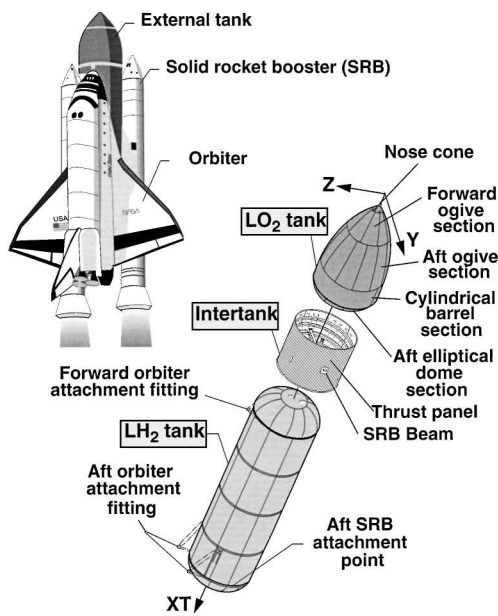[§]Head, Structural Mechanics Branch. Fellow AIAA.

Fig. 1   Space Shuttle external tank components.

a) Side view   b) Aft view

Fig. 2   Space Shuttle external LO$_2$ tank components; values of *XT* are given in inches.

paper also serves as an illustrative example of the use of large-scale numerical computation to characterize the response of a liquid-fuel launch vehicle. The modeling and analysis methods that are employed, and the insight provided by the results, should be applicable to the design of future liquid-fuel launch vehicles.

To address the objectives of the present paper, a brief overview of the SLWT tank structure and the details of the loading condition are presented first. Then, details of the finite element models, load simulation, and mesh convergence studies are summarized. Results of linear-bifurcation analyses are presented, and then results of nonlinear analyses for geometrically perfect and imperfect linear elastic shells are presented. The imperfection sensitivity results include a discussion of the effects of modal interactions associated with several nearly equal eigenvalues. In the presentation, generic aspects of the finite element model, analyses, and results that may be applicable to the design of future liquid-fuel launch vehicles are discussed.

Overview of the Structure

The Space Shuttle consists of the orbiter, two SRBs, and the external tank (ET), as shown in Fig. 1. The ET consists of an LO$_2$ tank, an LH$_2$ tank, and an intermediate structure called the intertank (Fig. 1). The intertank transmits the weight of the fuel, the ET structural weight, and the orbiter weight to the SRBs prior to launch, and transmits thrust loads from the SRBs and the orbiter to the ET during ascent. The SLWT LO$_2$ tank is a thin-walled monocoque shell that is made primarily of 2195 aluminum–lithium alloy. The LO$_2$ tank is approximately 49 ft long and has a maximum diameter of approximately 27.5 ft, as indicated in Fig. 2. The LO$_2$ tank consists of a forward-ogive section made from 8 gore panels, an aft-ogive section made from 12 gore panels, a cylindrical barrel section made from 4 barrel panels, and an aft elliptical dome section made from 12 gore panels. The coordinate systems used to locate the elements of the LO$_2$ tank and the intertank are also shown in Fig. 2. The coordinates (*XT, Y, Z*) are typically referred to as the global coordinate system of the ET, and axial positions along the tank are indicated by the coordinate value of *XT* in inches. For example, the location of the junction between the forward- and aft-ogive sections is indicated by writing $XT = 536.74$ in. Cylindrical coordinates are also used and are given by (*XT, r, θ*), where a positive value of θ is measured from the positive Z axis toward the positive Y axis, as shown in Fig. 2b.

The LO$_2$ tank also has a forward ring frame with a T-shaped cross section that is referred to herein as the T-ring frame, and an aft ring frame with a Y-shaped cross section that is referred to herein as the Y-ring frame (see Fig. 2a). These two ring frames support a baffle assembly that prevents the fuel from sloshing during ascent. The
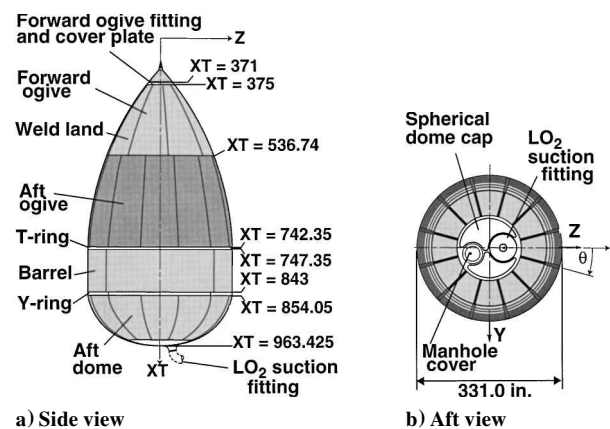
slosh baffle, a lightweight (approximately 455 lb), thin-walled structure, is supported by deep, thin-walled rings at each end that attach to the forward T-ring and the aft Y-ring frames. Other parts of the LO$_2$ tank include a nonstructural nose cone, a forged forward-ogive fitting and cover plate, an aft spherical dome cap that contains the LO$_2$ suction fitting and a covered manhole, and a vortex baffle attached to the base of the aft dome cap. The LO$_2$ tank gore and barrel panels are stretch formed, chemically milled, and then welded together. The panels are fabricated with substantial thickness tailoring to reduce structural weight. The panels are somewhat thicker at the welds to form a stiffenerlike region that is used as a weld land. The primary role of the weld lands is to compensate for any reduction in shell-wall strength that is caused by welding. Tapering the weld lands in thickness and width along their length reduces weight and alleviates stress concentrations in the shell that result from abrupt changes in thickness.

The intertank is a right circular cylinder that is made from 2090 aluminum–lithium and 7075 aluminum alloys and is shown in Fig. 1. The approximately 22.5-ft-long intertank has a diameter of approximately 27.5 ft and consists of six 45-deg curved panels that are stiffened longitudinally with external hat stiffeners and are referred to herein as skin-stringer panels. The intertank also has two massive, 45-deg curved panels, referred to as thrust panels (Fig. 1), that are located perpendicular to the Y-axis of the intertank and stiffened longitudinally with integrally machined external blade stiffeners. These eight panels are assembled into the intertank with mechanical fasteners and are attached to five large internal ring frames, a forward flange, and an aft flange. Longitudinal straps (referred to herein as roll ties) suppress lateral-torsional deflection of the ring frames. The main central ring frame, the thrust panels, and two thrust panel longerons are connected to each end of a tapered beam that is referred to herein as the SRB beam (Fig. 1). The SRB beam spans the diameter of the intertank along the Y axis and has a maximum depth (in the *XT* direction) of approximately 43 in. at its midspan. Forged fittings (referred to herein as SRB thrust fittings) that are incapable of transmitting moments are fastened to the ends of the SRB beam. The primary role of the thrust panels is to diffuse the large axial loads introduced by the SRBs into the intertank and then into the LO$_2$ tank shell wall. The SRB beam compensates for the eccentricity of the concentrated loads introduced by the SRBs. The SRB beam also supports loads that are normal to the intertank (parallel to the SRB beam) at the SRB attachment points. The intertank also has a 46 in. high × 52 in. wide frame-reinforced nonstructural access door located along the cylinder generator at approximately $\theta = 146$ deg.

Critical Loading Condition

The early booster ascent loading condition was identified and supplied by the members of the SLWT tank structural verification team at the NASA Marshall Space Flight Center and the Lockheed Martin Michoud Space Systems Division. This loading condition was identified as a worst-case loading condition that could cause

buckling of the forward ogive of the LO_2 tank, and, thus, no attempts are made in the present study to address issues of loading imperfections or perturbations. This critical loading condition occurs 69.66 s into flight and corresponds to an LO_2 tank that is approximately seven-eighths full and an acceleration field given by $a_X = -2.011\ g$, $a_Y = -0.049\ g$, and $a_Z = -0.440\ g$, where g is the magnitude of the gravitational acceleration. The X subscript in the first acceleration component corresponds to the XT direction and is used in the present paper for convenience. Details of this loading condition are shown in Figs. 3–6. The loads, shown schematically in Fig. 3, consist of the inertial loads of the structural mass and the LO_2 mass, the ullage pressure present inside the LO_2 tank, the aerodynamic pressure distribution on the exte-
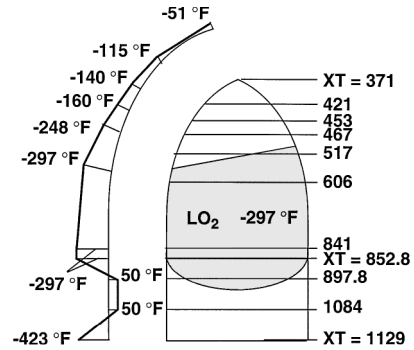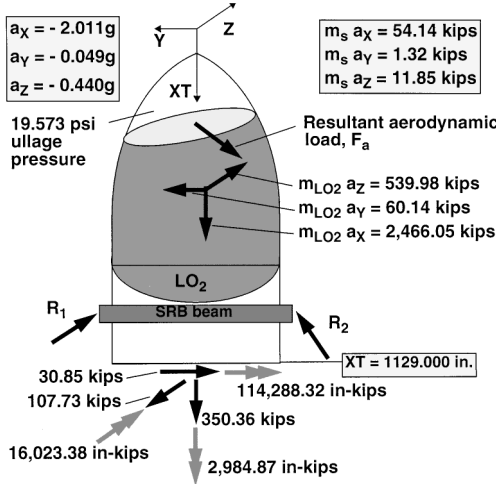

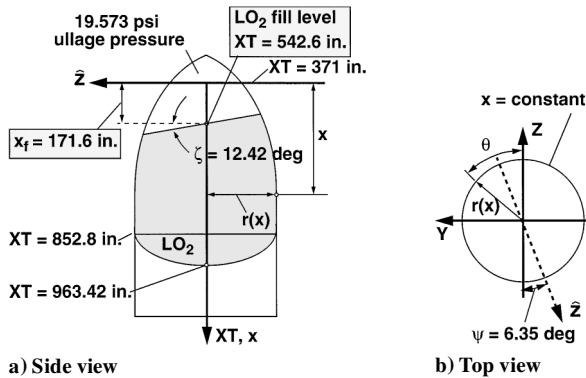**Fig. 3   Loads at 69.66 s into flight.**

Fig. 4 LO_2 pressure distribution at 69.66 s into flight.
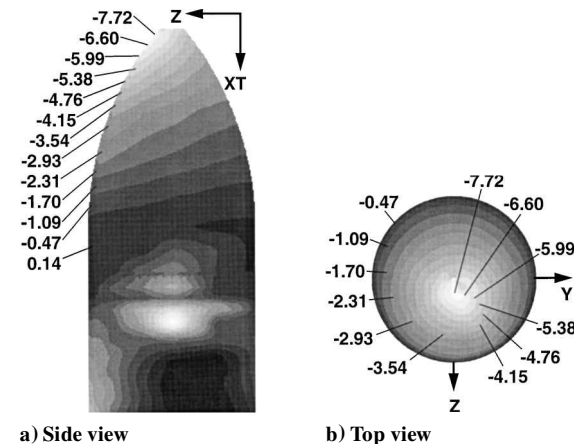
Fig. 5   Aerodynamic pressure distribution at 69.66 s into flight; values are given in pounds per square inch.

Fig. 6   Axisymmetric temperature profile at 69.66 s into flight; values of XT are given in inches.

rior surfaces of the ET, the LH_2 tank interface force and moment, and the thermal load associated with the cryogenic-fuel and aerodynamic heating. The inertial loads of the structural mass are given by $m_s a_X = 54.14$, $m_s a_Y = 1.32$, and $m_s a_Z = 11.85$ kips (1 kip $= 1000$ lb). Similarly, the inertial loads of the LO_2 mass are given by $m_{LO_2} a_X = 2,466.05$, $m_{LO_2} a_Y = 60.14$, and $m_{LO_2} a_Z = 539.98$ kips. The interface force and moment between the intertank and the LH_2 tank are given by $F = 350.36i - 30.85j - 107.73k$ kips and $M = 2,984.87i - 114,288.32j + 16,023.38k$ in.-kips, where i, j, and k are standard orthonormal base vectors associated with the XT, Y, and Z axes, respectively. The forces, R_1 and R_2, shown in Fig. 3, are the resultant forces at the SRB attachment points necessary to equilibrate all of the other loads on the structure.

As the Space Shuttle is accelerated, the LO_2 mass exerts pressure on the interior surface of the LO_2 tank shell wall. The resultant force of this pressure distribution corresponds to the inertial loads of the LO_2 that are given in Fig. 3. The pressure from the LO_2 mass and the ullage pressure are superimposed and the resulting pressure distribution on the interior surface of the LO_2 tank is approximated by the situation depicted in Fig. 4 in which the LO_2 and its container are subjected to rigid-body motion and flow effects are neglected.

This approximate pressure distribution on the interior surface of the LO_2 tank is given by

$$p(x, \theta) = p_u \qquad \text{for} \qquad x \le x_s \qquad (1)$$

$$p(x, \theta) = p_u - \gamma_{LO_2}(a_X/g)(x - x_s) \qquad \text{for} \qquad x > x_s \quad (2)$$

where x is a local axial coordinate that is measured from $XT = 371.00$ in., x_s is the local x coordinate of the surface of the fuel given by

$$x_s = x_f - r(x)[(a_Y/a_X)\sin\theta + (a_Z/a_X)\cos\theta] \qquad (3)$$

where $x_f = 171.6$ in. is a local x coordinate of the fill level ($XT = 542.60$ in.) and $r(x)$ is the horizontal or polar radius of the tank. The ullage pressure is given by $p_u = 19.573$ psi, and the specific weight of the LO_2 that was used in the present study is given by $\gamma_{LO_2} = 0.04123$ lb/in.[3]. The local $\hat{z}$ axis shown in Fig. 4b corresponds to the direction along which the free surface of the LO_2 has a maximum inclination angle relative to the y–z plane and is given by $\theta = 180$ deg $+ \psi$, where $\psi = \text{Tan}^{-1}(a_Y/a_Z) = 6.35$ deg. Similarly, the free surface of the LO_2 has an inclination angle in the x–$\hat{z}$ plane that is given by $\zeta = \text{Tan}^{-1}[\sqrt{(a_Y^2 + a_Z^2)}/|a_X|] = 12.42$ deg.

The aerodynamic pressure distribution on the exterior surfaces of the ET (all surfaces except the LO_2 tank aft dome section) was approximated by interpolating a grid of known pressure values given at specific (XT, θ) coordinates. The aerodynamic pressure distribution for the early booster ascent loading condition is shown in Fig. 5, where negative values correspond to inward pressure.

The temperature distribution that was used in the present study as an approximation associated with the cryogenic-fuel and aerodynamic heating is shown in Fig. 6. The temperature distribution shown in Fig. 6 is axisymmetric and varies along the surface meridians in a piecewise-linear manner. The warmest place on the LO_2

tank is the tip of the ogive section ($-51°$F), and the coldest is the barrel and the aft dome sections ($-297°$F). The coldest place on the intertank is at the LH$_2$ tank interface, given by $XT = 1129$ in. ($-423°$F). The nominal ambient temperature of the LO$_2$ tank and the intertank prior to fueling is $50°$F. This temperature was used in the present study as the temperature at which thermal stresses in the LO$_2$ tank are absent.

Analysis Code and Finite Element Modeling

The results of the linear-bifurcation buckling and nonlinear analyses were obtained with the STAGS nonlinear structural analysis code for general shells.[3] The STAGS code was chosen for analyzing the SLWT tank because of its robust state-of-the-art, nonlinear-equation solution algorithms and its general user-input capability that is convenient for modeling branched shells typically used for launch vehicles. The shell elements that were used to model the SLWT tank response are based on classical thin-shell theory. The use of these elements is justified because the ratio of the wall thickness to the minimum radius of curvature at each point of the undeformed LO$_2$ tank is much less than 0.1 and, as will be shown, because the ratio of the largest thickness of the shell wall that forms a given deformation pattern to the smallest characteristic length of the deformation pattern is less than 0.1 (Ref. 2). A description of the attributes of STAGS and how the features of STAGS were used in the present study to model the SLWT LO$_2$ tank and intertank are presented in Refs. 3 and 4. The finite element models of the SLWT tank that were used in the present study are very complex and include many structural details and skin thickness variations or tailoring used to reduce structural weight. The finite element modeling details for the SLWT LO$_2$ tank and intertank are lengthy and are not presented herein; they are discussed in Refs. 1, 2, and 4. Details of how the applied loads were simulated in the present study are presented subsequently.

Load Simulation

The basic approach used in the present study to simulate the actual early booster ascent loading condition is to apply all loads, accelerations, and associated inertial and LO$_2$ pressure loads illustrated in Figs. 3–5 to the model, except for the SRB interface loads. The nodes on the ends of the SRB beam, where the SRB forces act (see Fig. 3), were restrained so that the SRB interface forces become reactions and rigid-body motion is eliminated. The thermal load was applied by introducing the axisymmetric temperature distribution shown in Fig. 6 as a temperature change from a nominal initial uniform temperature of $50°$F. The applied loads were separated into two groups. The first group contains the pressure that acts on the shell wall because of the acceleration of the LO$_2$ mass, the structural-mass inertial loads, the inertial line loads that represent the acceleration of the slosh baffle mass that is located inside of the barrel section of the LO$_2$ tank, the aerodynamic pressure, and the LH$_2$ tank interface force and moment. This group of loads is treated as the primary source of destabilizing compressive stresses in the LO$_2$ tank that may occur at load levels greater than the corresponding operational load level. The second group of loads consists of the thermal load and the LO$_2$ tank ullage pressure. The loads in the second group are considered to be passive loads when determining the stability margin of safety of the LO$_2$ tank, and are constant in value throughout the analyses. In performing linear-bifurcation buckling and nonlinear analyses with STAGS, two load factors, p_a and p_b, were assigned to the first (active) and second (passive) load groups, respectively. Values of $p_a = p_b = 1$ correspond to the loading condition that was described earlier as the operational load level.

Results and Discussion

Three different finite element models were used in the present study to perform a limited convergence study in the analysis of the LO$_2$ tank subjected to the early booster ascent loading condition. As a first step toward identifying an adequate model with as few degrees of freedom as necessary, elastic, linear-bifurcation buckling analyses were conducted. The passive loads associated with load factor p_b were applied to the STAGS models as a linear prebuckling stress state ($p_b = 1$), and the active (destabilizing) loads associated with load factor p_a were used to obtain the minimum eigenvalue.
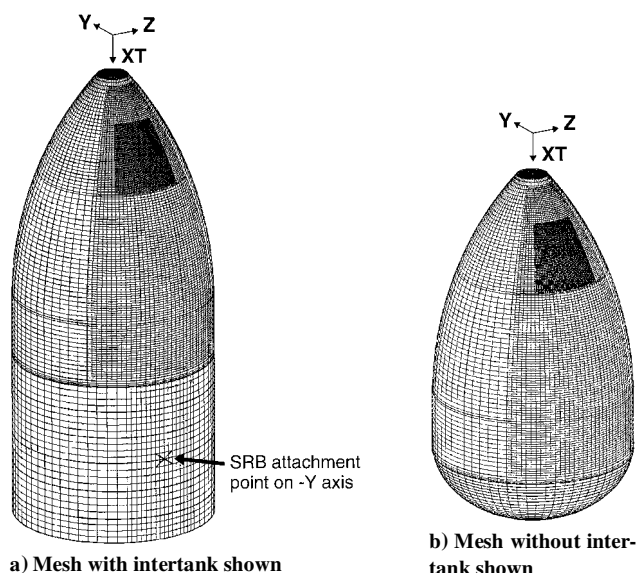

a) Mesh with intertank shown

b) Mesh without intertank shown

Fig. 7 Finite element mesh; 125,000 degrees of freedom.
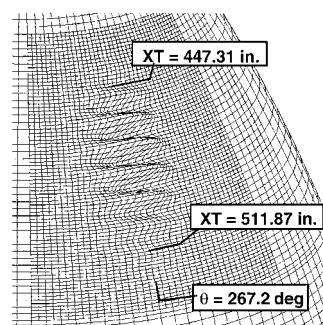

Fig. 8 Linear-bifurcation buckling mode; 125,000 degrees of freedom, $p_a = 2.182$ and $p_b = 1.0$.

The models that were investigated had 49,000, 96,000, and 125,000 degrees of freedom. The model that was identified as adequate for predicting the linear-bifurcation buckling behavior is shown in Fig. 7 and corresponds to 125,000 degrees of freedom.

The first linear-bifurcation mode (referred to herein as the linear-bifurcation buckling mode) for the geometrically perfect shell is shown in Fig. 8 for the STAGS model with 125,000 degrees of freedom. The eigenvalue for this model corresponds to active loads that are approximately 2.182 times the magnitude of the corresponding operational loads shown in Figs. 3–5. This buckling mode is a localized, short-wavelength wrinkle in the aft part of the forward ogive that extends from approximately $XT = 447.31$ to 511.87 in. and is centered circumferentially on $\theta = 267.2$ deg (near the negative Y axis). The second through eighth linear-bifurcation modes are also localized, short-wavelength modes, similar to the mode shown in Fig. 8, with eigenvalues equal to 2.183, 2.207, 2.209, 2.244, 2.246, 2.260, and 2.260, respectively, that are all less than 4% higher than the lowest eigenvalue. The second through sixth linear-bifurcation modes are also in the aft part of the forward ogive and centered on $\theta = 267.2$ deg. The seventh and eighth modes are located in the aft part of the forward ogive, but are on the opposite side of the tank (near the positive Y axis) and centered on $\theta = -2.8$ deg.

The nearly equal values of the first eight eigenvalues, the short wavelength of the linear-bifurcation modes, and the locations of the linear-bifurcation modes led to the dense mesh refinement of the forward ogive that is shown in Figs. 7 and 8. The mesh refinement that is shown centered on the negative Y axis was also applied on the positive Y-axis side of the model. Meridional and circumferential mesh refinement of the forward-ogive, aft-ogive, and barrel sections was facilitated by the use of the five-node and seven-node rectangular transition elements available in STAGS.[4] The 96,000- and 125,000-degree-of-freedom models have the same general mesh arrangement shown in Fig. 7, but the level of refinement of the aft part of the forward ogive shown in Figs. 7 and 8 for the 125,000-degree-of-freedom model is essentially twice that of

the 96,000-degree-of-freedom model. The lowest eigenvalues for the 96,000- and 125,000-degree-of-freedom models are given by $p_a = 2.204$ and 2.182, respectively. The smoothness of the buckling mode shown in Fig. 8 and the 1% difference in the eigenvalues indicate that the 125,000-degree-of-freedom model is adequate for representing the linear-bifurcation behavior of the LO$_2$ tank for this loading condition. In addition, the ratio of the largest thickness in the area of the buckling mode shown in Fig. 8 to its smallest characteristic length is less than 0.1, which suggests that finite elements that are based on classical thin-shell theory are adequate.

The 96,000- and 125,000-degree-of-freedom models were also used to obtain nonlinear solutions for geometrically perfect and imperfect shells. These solutions, which are in good agreement (within 1% of one another), indicate that the 125,000-degree-of-freedom model adequately represents the nonlinear behavior of the LO$_2$ tank for this loading condition. Thus, all subsequent results presented in this section were obtained with the 125,000-degree-of-freedom model.

The meridional stress resultant distribution in the LO$_2$ tank (on the negative Y-axis side of the tank and given in units of pounds per inch) that was obtained from nonlinear analyses is shown in Fig. 9 for values of $p_a = p_b = 1$ and for $p_a = 2.216$ and $p_b = 1$. The darker shading shown in Fig. 9 corresponds to meridional tension that resists primarily the axial acceleration of the LO$_2$ mass. The lighter shading shown in Fig. 9 corresponds to meridional compression resulting from the SRB interface loads (reaction forces) that are applied in the intertank and dissipate into the LO$_2$ tank along the $(+Y)$ and $(-Y)$ axes. The highest values of meridional compression are in the aft end of the barrel near $\theta = 90$ and 270 deg. The average shell wall thickness in and around this region is 0.381 in. These results show that the meridional stress in the location of the buckling modes is tensile for $p_a = 1$, but at the higher load value the meridional stress becomes compressive in the forward ogive in a region where the average wall thickness is 0.093 in., and this meridional compression causes this region to buckle. The circumferential stress resultants in the LO$_2$ tank are shown in Fig. 10 for values of $p_a = p_b = 1$ and for $p_a = 2.216$ and $p_b = 1$. These results show that the entire LO$_2$ tank exhibits circumferential tension that resists primarily the LO$_2$ pressure and ullage pressure. The circumferential tension, which has a stabilizing effect on the shell, is smallest in the forward ogive. The small circumferential tension in the location of the buckling mode, combined with the meridional compression, is responsible for the shortness of the wavelength of the eight linear-bifurcation modes.

An important concern that arose during the course of the present study is the possibility of high sensitivity to initial geometric imperfections that may be affected by the presence of nearly equal eigenvalues of the linear-bifurcation modes. This sensitivity could lead to a premature collapse mode for the forward ogive. To address imperfection sensitivity, nonlinear analyses were conducted for an imperfect shell with an imperfection shape in the form of a linear combination of the first eight linear-bifurcation modes, described earlier. Mathematically, this set of modes can be viewed loosely as a basis for an isotropic imperfection space, similar to a basis of a vector space. The linear-bifurcation modes were selected because they represent configurations that the structure has an intrinsic affinity to deform into, provided that there are no substantial nonlinear prebuckling effects present. That is, in the absence of substantial nonlinear prebuckling effects, the linear-bifurcation eigenvalues represent when (at what load level) and where (what configurations) strong interactions between compressive membrane stresses and normal displacements are likely to be present. In addition, the eight-mode imperfection was selected because of the statement given by Bushnell[5] that suggests that premature failure of shell structures that exhibit a short-wavelength response can be activated or triggered by imperfections with a similar short-wavelength shape. Thus, the eight-mode imperfection is expected to represent adequately a preferred direction of departure from the primary equilibrium path should the structure have a tendency to do so.

Results are presented in Figs. 11–13 that show the nonlinear deformations that were obtained from STAGS analyses of a geometrically perfect shell and a geometrically imperfect shell with an imperfection-amplitude-to-wall-thickness ratio $A/t_1 = 1$, respectively. The thickness t_1 in the ratio A/t_1 is the average wall thickness of the forward ogive where the buckling mode is located ($t_1 = 0.093$ in.). The results in Figs. 11–13 are for nonlinear solutions that were obtained by increasing the load factors p_a and p_b simultaneously to a value of one and then holding p_b constant while increasing the magnitude of the load factor p_a. The exaggerated, deformed shape of the LO$_2$ tank obtained from nonlinear analysis of a geometrically perfect shell with the load factors $p_a = 2.743$ and $p_b = 1.0$ is shown in Fig. 11. The load level for this solution is approximately 2.74 times the operational load level and approximately 1.26 times the linear-bifurcation buckling load level. The deformed shape shown in Fig. 11 displays a short-wavelength bending response in the forward ogive and a bending response with a longer
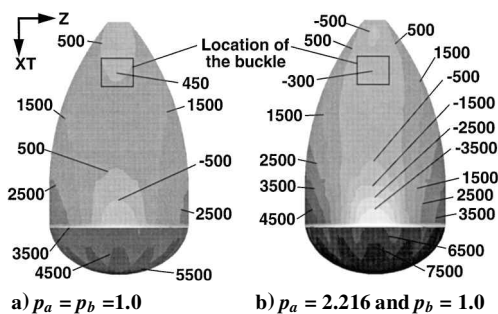

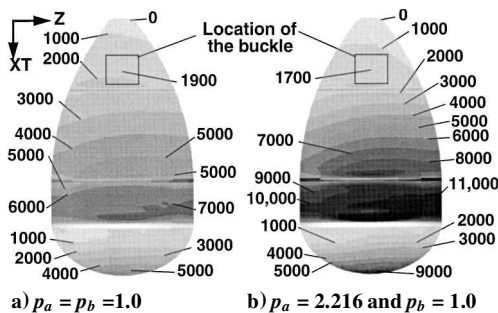**Fig. 9   Meridional stress resultants in LO$_2$ tank (pounds per inch).**

Fig. 10   Circumferential stress resultants in LO$_2$ tank (pounds per inch).
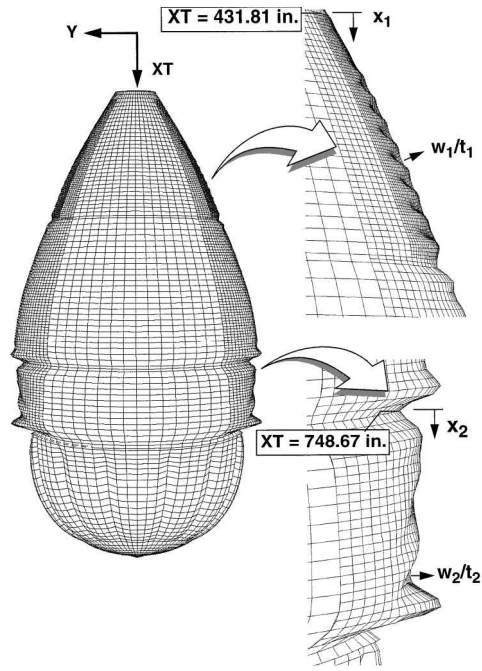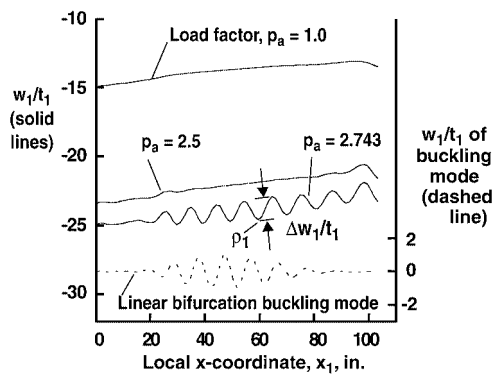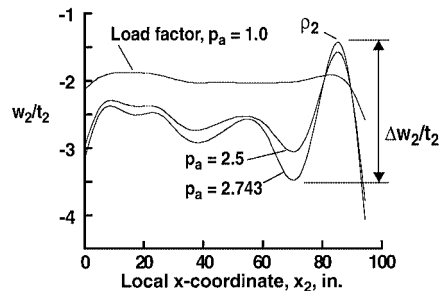

Fig. 11   Deformed shape of LO$_2$ tank from nonlinear analysis of geometrically perfect shell; $p_a = 2.743$ and $p_b = 1.0$.

a) Forward ogive: $t_1 = 0.093$ in. and $\theta = 267.2$ deg

b) Barrel: $t_2 = 0.381$ in. and $\theta = 270.0$ deg

Fig. 12 Nondimensional normal displacement w/t of geometrically perfect shell, forward ogive and barrel sections.
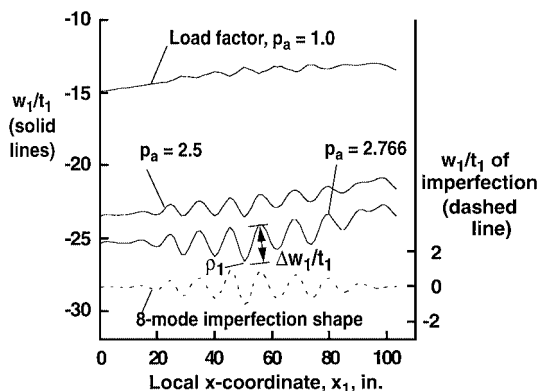

Fig. 13 Nondimensional normal displacement w_1/t_1 of geometrically imperfect forward ogive; imperfection-amplitude-to-wall-thickness $A/t_1 = 1$, $t_1 = 0.093$ in., and $\theta = 267.2$ deg.

wavelength in the barrel. The bending deformations are present near the $(+Y)$ and $(-Y)$ axes ($\theta = 90$ and 270 deg, respectively), but are largest for $\theta \approx 270$ deg. In Fig. 11, local x coordinates, x_1 and x_2, and nondimensional normal displacements, w_1/t_1 and w_2/t_2, are defined in the forward-ogive and barrel sections, respectively. The normal displacements are normalized by the average wall thickness in the region where the bending deformation occurs; that is, $t_1 = 0.093$ in. in the forward ogive and $t_2 = 0.381$ in. in the barrel.

Results are presented in Fig. 12 that show the nondimensional normal displacements of the geometrically perfect shell along a meridian for values of the load factor p_a equal to 1.0, 2.5, and 2.743. The nondimensional normal displacements along a meridian of the forward-ogive shell wall at $\theta = 267.2$ deg are represented by the solid lines in Fig. 12a. Overall, negative values of the normal displacements are indicated by the left-hand ordinate for these three load factors. These results are negative because of the LO_2 thermal load (shrinkage) and meridional compression and cross-sectional ovalization of the ET caused by the LO_2 pressure load and the discrete SRB interface loads, respectively. The linear-bifurcation buckling mode is represented by the dashed line in Fig. 12a, with the

normalized amplitude given by the right-hand ordinate of Fig. 12a. The nondimensional normal displacements along the meridian of the barrel shell wall at $\theta = 270.0$ deg for the three values of the load factor are shown in Fig. 12b.

The solid lines shown in Fig. 12a indicate development of a short-wavelength bending response in the forward ogive. At the operational load level given by $p_a = 1$, the results predict minimal bending deformations. At a load level of $p_a = 2.5$, which is greater than the linear-bifurcation buckling load level ($p_a = 2.182$), the results predict the onset of a nonlinear bending response in the locations given by $x_1 = 25$ and 100 in. As the load is increased to $p_a = 2.743$, substantial bending deformations (indicated by the waviness in the curves) develop and grow in the forward ogive, which reduces the apparent meridional stiffness of the forward ogive. The pattern of the nonlinear deformation is similar to the linear-bifurcation buckling mode.

The solid lines shown in Fig. 12b indicate the development of a bending response in the LO_2 barrel with a longer wavelength than the bending response in the forward ogive. At the operational load level given by $p_a = 1$, the results predict a significant bending boundary layer at the aft end of the barrel. For $p_a = 2.5$, the results predict that the nonlinear bending response has grown in amplitude and extends along the entire length of the barrel, which reduces the apparent meridional stiffness of the barrel. As the load level is increased to $p_a = 2.743$, the bending deformations in the barrel grow to an amplitude of approximately two times the average wall thickness. The bending response at the aft end of the barrel is attributed to three interacting load effects. First, the LO_2 pressure causes radially outward bulging around the stiff joint at the intersection of the barrel, aft dome, and intertank. Second, meridional tension in the aft dome creates a moment on this joint about the circumferential coordinate line. Third, the SRB interface loads are transmitted through the intertank thrust panels and create compressive loads in the barrel at the circumferential locations centered on $\theta = 90$ and 270 deg (see Fig. 9). As the load factor increases, all of these loading effects increase in magnitude, and coupling between the meridional compression and the bending response causes nonlinear growth of the deformations.

Results are presented in Fig. 13 that show the nonlinear deformations in the forward ogive that were obtained from STAGS analysis of a geometrically imperfect shell with an imperfection-amplitude-to-wall-thickness ratio $A/t_1 = 1$ ($t_1 = 0.093$ in.). The eight-mode imperfection that was described earlier in the present paper was used, with the imperfection shape given by -0.0325 times the summation of the first six eigenvectors, plus -0.0656 times the summation of the seventh and eighth eigenvectors. The negative-valued linear combination was used as the imperfection shape because it was found to provide a stronger nonlinear interaction with the compressive stresses in the shell wall than the positive-valued linear combination. The multiplication factors were selected to provide an imperfection shape in the forward ogive such that the regions centered on $\theta = 90$ and 270 deg both had an imperfection-amplitude-to-wall- thickness ratio $A/t_1 = 1$. The nondimensional normal displacements along the meridian of the forward-ogive shell wall at $\theta = 267.2$ deg, for values of the load factor p_a equal to 1.0, 2.5, and 2.766, are represented by the solid lines in Fig. 13. The shape of the eight-mode imperfection along the meridian at $\theta = 267.2$ deg is represented by the dashed line.

The nonlinear deformation pattern of the geometrically imperfect ogive shown in Fig. 13 is very similar to the shape of the geometric imperfection. Comparison of the results for the geometrically perfect and geometrically imperfect forward ogive, shown by the solid lines in Figs. 12a and 13, respectively, indicates that the eight-mode imperfection amplifies the severity of the bending deformation in the forward ogive and causes the growth of the bending deformations to form at lower load levels. The nondimensional normal displacements in the barrel of the geometrically imperfect shell are not presented because the imperfection in the forward ogive has very little effect on the deformation in the barrel, and the results obtained are essentially the same as the geometrically perfect shell results shown in Fig. 12b. The deformation patterns shown in Figs. 12 and 13 confirm that the ratio of the largest thickness in the
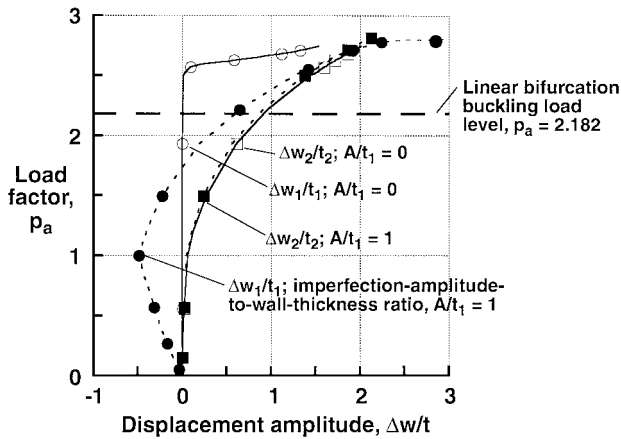
Fig. 14 Local nondimensional normal displacement amplitude, $\Delta w/t$, in forward-ogive and barrel sections for geometrically perfect and geometrically imperfect forward ogive. Forward ogive: $t_1 = 0.093$ in., for $A/t_1 = 0$, Δw_1 is at $XT = 491$ in., and $\theta = 267.2$ deg; for $A/t_1 = 1$, Δw_1 is at $XT = 482$ in., and $\theta = 267.2$ deg; barrel: $t_2 = 0.381$ in., Δw_2 is at $XT = 827$ in., and $\theta = 270.0$ deg.

area of the deformation to the smallest characteristic length of the deformation pattern is less than 0.1, which suggests that finite elements that are based on classical thin-shell theory are adequate. In addition, the von Mises stresses in the forward ogive and the barrel were calculated for the higher load factors shown in Figs. 12 and 13 and were found to be below the approximately 70-ksi yield stress of the aluminum–lithium material.

The predicted growth of the bending deformations and the associated reductions in the apparent meridional stiffness of the forward ogive and the barrel of the geometrically perfect and imperfect shells are shown more explicitly in Fig. 14. The maximum amplitude of the undulations in the normal displacements in the forward ogive and the barrel, $\Delta w_1/t_1$ and $\Delta w_2/t_2$ (shown graphically in Figs. 12 and 13) are given as a function of the load factor p_a in Fig. 14. The two solid curves presented in Fig. 14 correspond to deformations of the forward ogive (unfilled circles) and barrel (unfilled squares) of the geometrically perfect shell. Similarly, the two dashed curves presented in Fig. 14 correspond to deformations of the forward ogive (filled circles) and barrel (filled squares) of the geometrically imperfect shell with $A/t_1 = 1$. The horizontal dashed line shown in Fig. 14 represents the linear-bifurcation buckling load level ($p_a = 2.182$).

The results shown in Fig. 14 indicate that the bending deformations in the forward ogive of the geometrically perfect shell are very small for values of the load factor $p_a < 2.6$, but increase rapidly for $p_a > 2.6$. The results for the geometrically imperfect shell predict that the bending deformations in the forward ogive are negative for values of the load factor $p_a < 1.8$. These negative values correspond to flattening of the imperfection shape that is caused by tensile meridional and circumferential stresses. For $p_a > 1.8$, $\Delta w_1/t_1$ becomes positive and increases monotonically. This behavior is the result of the fact that the meridional stresses in the forward ogive become compressive for $p_a > 1.8$. The results presented in Fig. 14 also predict that the bending response in the barrel ($\Delta w_2/t_2$) is small at the operational load level ($p_a = 1.0$), increases monotonically for values of the load factor $p_a > 1.0$, and is virtually unaffected by the imperfection in the forward ogive.

All of the results shown in Fig. 14 generally show a monotonically increasing nonlinear response and predict that the shell can support loads greater than the critical buckling load predicted by an elastic, linear-bifurcation buckling analysis. From a generic point of view, the results indicate that a design based on a linear-bifurcation buckling analysis and buckling-load knockdown factor would be overly conservative. The nonlinear analyses predict that as the load factor p_a increases, Δw increases (reducing the apparent meridional stiffness), and the slope of the load vs Δw curve decreases but remains positive valued. The reduction in slope of the load vs Δw curve indicates an increase in the rate of displacement growth, whereas the positive-valued slope indicates that the apparent meridional stiff-

ness is positive valued and that the deformation growth is stable. This type of response is similar to the response presented for the prelaunch loading condition with full LO_2 and LH_2 tanks[1] and to the response reported by Stevens et al.[6] for cylindrical shells subjected to combined internal pressure and a pure bending moment. The results in Ref. 6 indicate that the amplitude of the short-wavelength deflection grows rapidly as the load increases and approaches a critical value. At the critical value of the load, the load-deflection response curve approaches a horizontal tangent that corresponds to a local collapse mode of the cylinder. Mathematically, the horizontal tangent indicates that unbounded growth of the displacement occurs for an infinitesimal increase in the load. It is expected that the curves shown in Fig. 14 would approach a horizontal tangent as the load factor increases until a redistribution in load occurs within the forward-ogive and barrel sections. As a horizontal tangent in a load vs displacement amplitude curve is approached, the region of the shell containing the bending deformations becomes incapable of supporting additional load, and the compressive load is redistributed to another portion of the shell. If other parts of the shell cannot support the redistributed compressive load or if excessive yielding occurs, the shell will collapse.

Despite the concerns about acute imperfection sensitivity that is sometimes affected by the presence of several nearly equal linear-bifurcation eigenvalues, the results presented in Figs. 13 and 14 indicate a stable nonlinear response for the imperfect shell, which has a relatively large imperfection amplitude. Moreover, the results indicate the forward-ogive and barrel sections retain a positive-valued, apparent meridional stiffness as the bending deformations develop that supports the insensitivity of the collapse load to imperfections in the forward ogive. Because no eigenvectors were found that correspond to bifurcation buckling modes in the barrel, imperfection sensitivity of the barrel was not quantified. The nonlinear prebuckling deformations in the barrel were characteristic of stable growth of a bending boundary layer that is driven by the loading. The deformations in the barrel did not exhibit limit-point or bifurcation-type behavior and, thus, should not be sensitive to imperfections. The stability of the wrinklelike deformation states in the forward ogive and the barrel is at least partially attributed to the presence of tensile circumferential stress resultants in these regions. Furthermore, the meridional compression region is a local region that is more likely to cause a benign internal load redistribution in the presence of nonlinear prebuckling deformations than a sudden mode change or collapse. The behavior of the LO_2 tank is significantly different from that of a compression-loaded cylinder or an externally pressurized sphere that exhibit several nearly equal, or a multiplicity of, linear-bifurcation eigenvalues. A major difference is that the regions of compression of the LO_2 tank do not fully envelop the shell, unlike the compression-loaded cylinder or the externally pressurized sphere. This difference facilitates load redistribution in the LO_2 tank without shell collapse or a mode change. Conversely, if a future launch vehicle shell structure was to experience compressive stresses over a larger portion of its area, an increased imperfection sensitivity caused by modal interaction may be present.

Although the results presented in Figs. 12–14 predict that the SLWT tank will not collapse for load levels below approximately 2.6 times the operational load level, the results also indicate that large local bending deformations may occur for loads that are much smaller than the local collapse load. These local bending deformations may cause the TPS to debond from the shell wall and fail. This mode of failure is of great importance in the design of the TPS for contemporary space vehicles. The results presented in Fig. 15 give approximate estimates of the local radii of curvature, ρ_1 and ρ_2 (identified in Figs. 12 and 13), for the bending deformation in the forward-ogive and barrel sections, respectively. The local radius of curvature ρ was estimated by $\rho = |\kappa_x|^{-1}$, where κ_x is the curvature in the meridional direction of the finite element closest to the crest of the deformation pattern. The two solid curves presented in Fig. 15 correspond to bending deformations of the forward ogive (unfilled circles) and barrel (unfilled squares) of the geometrically perfect shell. Similarly, the two dashed curves presented in Fig. 15 correspond to bending deformations of the forward ogive (filled circles) and barrel (filled squares) of the geometrically imperfect shell
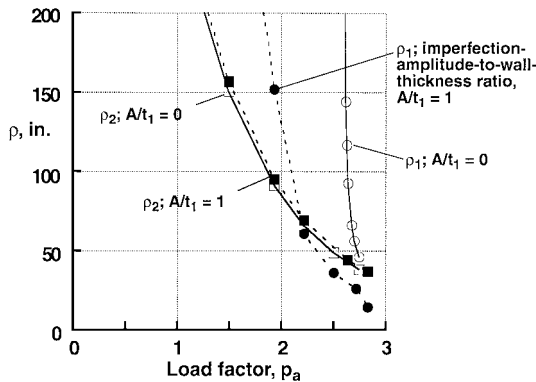
Fig. 15 Local radii of curvature ρ of bending deformation in forward-ogive and barrel sections for geometrically perfect and geometrically imperfect forward ogive. Forward ogive: $t_1 = 0.093$ in., for $A/t_1 = 0$, ρ_1 is at $XT = 491$ in., and $\theta = 267.2$ deg; for $A/t_1 = 1$, ρ_1 is at $XT = 482$ in., and $\theta = 267.2$ deg; barrel: ρ_2 is at $XT = 833$ in., and $\theta = 270.0$ deg.

with $A/t_1 = 1$. The results in Fig. 15 demonstrate that the geometric imperfection amplitude has a significant influence on the local radius of curvature of the forward ogive. For example, if a given TPS is known to debond from the shell wall at a value of $\rho = 100$ in., the maximum load factor before debonding occurs in the forward ogive is reduced from a value of approximately 2.6 for the geometrically perfect shell to 2.1 for the geometrically imperfect shell with $A/t_1 = 1$. However, a large-amplitude, short-wavelength imperfection of this type is unlikely to be present in a piece of high-precision flight hardware. Thus, the radius-of-curvature results for the perfect shell are more practical than the corresponding results for the imperfect shell because such large imperfections would most likely be identified during inspection of the shell. The results in Fig. 15 indicate that debonding of the TPS is more likely to first occur in the barrel. For the example given, with an allowable $\rho = 100$ in., the results predict that debonding of the TPS would occur at a load factor of approximately 1.9.

Concluding Remarks

Elastic, linear-bifurcation and nonlinear analyses of the Space Shuttle SLWT LO_2 tank have been presented. The loading details for an important early booster ascent loading condition have been described, and the method used to simulate the loading condition has been discussed. Results have been presented herein that were obtained from complex, large-scale finite element models of a portion of the Space Shuttle SLWT tank. These results for thin-walled linear elastic shells that are subjected to combined mechanical and thermal loads illustrate an important type of response mode that may be encountered in the design of other liquid-fuel launch vehicles. In addition, the results demonstrate that large-scale, high-fidelity, finite element models are generally required to predict accurately the linear-bifurcation and nonlinear responses, because the localized, short-wavelength deformation patterns are small compared to the overall size of the structure. Overly coarse, finite element models could predict an entirely different, and inaccurate, response mode.

For the early booster ascent loading condition, linear-bifurcation analyses yielded several nearly equal eigenvalues that correspond to local buckling modes. However, the nonlinear analyses yielded a response that is characterized by short-wavelength bending deformations in the forward-ogive and barrel sections of the LO_2 tank

that grow in amplitude in a stable manner with increasing load. The overall response of the structure is insensitive to initial shell-wall geometric imperfections because the localized nature of the compressive stresses in the shell facilitates stress redistribution instead of collapse of the shell. The LO_2 tank does not exhibit a nonlinear collapse mode associated with the interaction of nearly equal linear-bifurcation modes in the forward ogive for load levels below approximately 2.6 times the operational load level, or 19% higher than the critical buckling load predicted by an elastic, linear-bifurcation buckling analysis. An important consequence of these results, that may be applicable to the design of future liquid-fuel launch vehicles, is that a design based on the traditional approach of computing a linear-bifurcation buckling load and accounting for imperfection sensitivity with a buckling-load knockdown factor is likely to be overly conservative. This conclusion is especially true if buckling-load knockdown factors are not well known and must be contrived in some manner.

The local bending deformations that the nonlinear analyses predict for the forward-ogive and barrel sections do not cause general instability, but may cause failure of the TPS. To address this concern, results have been presented that can be used to estimate the load level at which TPS failure is likely to occur. The results do predict that TPS failure may occur at load levels less than the load level corresponding to structural collapse, and that the severity of some of the local bending deformations is significantly affected by the localized initial geometric imperfection. The method that was used to assess failure of the TPS requires a nonlinear analysis to predict accurately the shell wall deformations, and constitutes a method that can be used to assess the performance of TPS systems for future launch vehicles.

References

[1]Nemeth, M. P., Britt, V. O., Collins, T. J., and Starnes, J. H., Jr., "Nonlinear Analysis of the Space Shuttle Superlightweight External Fuel Tank," NASA TP-3616, Dec. 1996.

[2]Nemeth, M. P., Britt, V. O., Young, R. D., Collins, T. J., and Starnes, J. H., Jr.,"Nonlinear Behavior of Space Shuttle Superlightweight Liquid-Oxygen Tank Under Prelaunch Loads," *Journal of Spacecraft and Rockets*, Vol. 36, No. 6, 1999, pp. 788–803.

[3]Brogan, F. A., Rankin, C. C., and Cabiness, H. D., "STAGS User Manual, Version 3.1," Lockheed Martin Missiles and Space Co., Rept. LMSC P032594, Palo Alto, CA, March 1994.

[4]Young, R. D., and Rankin, C. C., "Modeling and Nonlinear Structural Analysis of a Large-Scale Launch Vehicle," *Journal of Spacecraft and Rockets*, Vol. 36, No. 6, 1999, pp. 804–811.

[5]Bushnell, D., "Static Collapse: A Survey of Methods and Modes of Behavior," *Collapse Analysis of Structures*, PVP-Vol. 84, American Society of Mechanical Engineers, Fairfield, NJ, 1984, pp. 30–32.

[6]Stephens, W. B., Starnes, J. H., Jr., and Almroth, B. O., "Collapse of Long Cylindrical Shells Under Combined Bending and Pressure Loads," *AIAA Journal*, Vol. 13, No. 1, 1975, pp. 20–25.